Three-Dimensional High-Resolution Space-Borne ISAR Imaging With Compact Antenna Configuration for Large Rotational Angle

Rui Gong , Ling Wang , and Daiyin Zhu

Abstract—Space situation awareness (SSA) has gained much more attention in the last decades due to the increasing number of spacecraft in space, which provides powerful space surveillance, and hence, ensures the safe flight of spacecraft. Inverse synthetic aperture radar (ISAR) is an effective tool for uncooperative target recognition and has been widely used in ground-based SSA systems. Due to the increasing usage of small spacecraft in missions and the similar appearance of most spacecraft, the high-resolution imaging is more highly needed for reliable spacecraft recognition than before, which is also desired by the component-level recognition. Furthermore, the 3-D image reconstruction of spacecraft is very helpful in evaluating the structures due to the addition of the 3-D information, and hence, has become a very promising tool for deep target analysis. This article proposes a high-resolution spaceborne 3-D ISAR imaging method with fewer requirements on the antenna configuration and high computational efficiency. First, dedicated processing is designed to get high azimuthal resolution using large target-to-radar rotational angle accumulation. We address associated issues including the migration through resolution cell phenomenon and the high-order azimuthal phase modulation leading to defocusing of the resultant spacecraft images. Second, with the generated high-resolution 2-D images, we use dual-antenna interferometric processing to acquire the 3-D coordinates. To get precise coordinates of scatterers in both vertical and horizontal directions, the cross-range scaling technique is used. Finally, interferometric processing is used for locating the targets' height coordinates. Simulation results indicate that the presented method can provide 3-D images of spacecraft of higher resolution with a simple system structure than the traditional interferometric ISAR image methods.

Index Terms—Interferometric inverse synthetic aperture radar (InISAR), polar format algorithm (PFA), space targets, 3-D imaging.

The authors are with the Key Laboratory of Radar Imaging and Microwave Photonics, Ministry of Education, College of Electronic and Information Engineering, Nanjing University of Aeronautics and Astronautics, Nanjing 211106, China (e-mail: gongrui1008@nuaa.edu.cn; tulip_wling@nuaa.edu.cn; zhudy@nuaa.edu.cn).

I. INTRODUCTION

RECENTLY, along with the unceasing progress in space technology, the number of on-orbit spacecraft has increased significantly in the past few years. To meet the requirements of space activities, improving the space situation awareness (SSA) needs to be given higher priority . It is essential to observe and identify space targets, which guides the space targets management and collision warning of on-orbit spacecraft [1]. Obtaining the clear image of space targets is a precondition for automatic target classification and recognition.

Inverse synthetic aperture radar (ISAR) is considered as one of the most effective tool in space targets recognition for its high-resolution 2-D imaging ability. The imaging algorithms have been deeply investigated in the past few decades [2], [3], [4], [5], [6], [7], [8]. All the time, ISAR systems attaches importance to the wide bandwidth, high carrier frequency, multipolarization, networking, and distribution capability, which have guided the progress and development of the ISAR imaging technique. Currently, two aspects of the improvement of ISAR imaging technology could be described: enriching the target information and improving the image quality. Thus, the multidimensional imaging and high-precision imaging are needed.

A 3-D image of a moving target can provide real geometrical structure characteristics of the target, which is conducive to the target's classification and identification. ISAR 3-D imaging can be divided into two categories. One aims at forming 3-D ISAR images through ISAR image sequences obtained by a single antenna with a long observation time. Nevertheless, the target motion states may change during this period. This could pose a challenge to integrate data coherently. The other recovers the information in horizontal and altitude dimensions using the interferometric technique [9], [10], [11], [12], [13], which requires a receiving system with at least two antennas.

Most space targets, such as three-axis stabilized satellites, have their equivalent rotations formed by spin motion and relative tangential motion. They are not maneuvering but moving with a steady attitude, allowing for the extended coherent integration time . High-resolution ISAR images require large relative rotational angles, which can only be produced by either a quick rotation velocity or a long observation time. Nevertheless, the image quality is seriously damaged by the highly Doppler frequency modulation (DFM) and the large migration through resolution cell (MTRC), which are induced by the large relative

rotational angle. There are numerous algorithms that have been proposed to address this issue. In [14], the large observation angle is divided into several subapertures to obtain the images from different perspectives, which shows that the different scatterers appear in different subaperture images and demonstrates the essentiality of high-performance space observation for a space target recognition. Wang et al. [15] apply the backprojection algorithm to the ISAR imaging and obtain expected high-resolution results in simulation, which assumes that the rotational vector of the target is already estimated. In addition, several iterations of phase compensation processing would lead to a large computational quantity. In [16], the translational and rotational motion parameters are estimated to compensate the echo. The focused ISAR image is achieved, whereas the series of optimizations in the parameter estimation implies a high computational complexity. In addition, the aforementioned algorithms are proposed for 2-D ISAR imagery, which cannot be directly applied in interferometric inverse synthetic aperture radar (InISAR) due to the incomplete preserved phase information.

The existing InSAR algorithms aim for small rotational angle, which cannot satisfy the high accuracy requirement of the subsequent recognition. For overcoming the difficulties when the relative rotational angle is large, we presented an InISAR imaging method with compact antenna configuration during which the high-resolution 3-D image of the target is formed. The polar format algorithm (PFA) is an algorithm extensively used in spotlight SAR imaging to eliminate MTRC caused by the radar motion radically. We employed the PFA in ISAR imaging to eliminate MTRC induced by the large relative rotational angle. Besides, we adopt the second-order local polynomial Fourier transform (SO-LPFT) for estimating the chirp rate. SO-LPFT is an effective time–frequency method, which maximizes the cross term suppression while maintaining the time–frequency resolution. Thus, we perform SO-LPFT to reduce the azimuth defocusing. At last, the 3-D image of the space moving target is rebuilt by the interferometric technique. In addition, we utilize the 3-D imaging algorithm with dual antenna for reconstructing the target [17], which can simplify the radar system and reduce the number of antennas.

The main contributions of this article are listed as follows.

1) The PFA and SO-LPFT are employed to correct MTRC and remove DFM induced by the large rotational angle. Thus, the interferometric phases are preserved well. The errors of the resultant 3-D reconstruction are smaller than those of previous RD-based 3-D imaging methods. The proposed method has obvious superiority even under the actual mutual motion scenarios between target and radar.

2) Our method is single-baseline based and has a low computational complexity as compared to the widely used L-type double-baseline-based 3-D imaging method. The parameters needed by the 3-D imaging can be acquired by antenna A and shared to antenna B, leading to less computation.

3) As we all known, angle glint is regarded as a limitation of the InISAR imagery. The proposed method makes the projection of each two scatterers different through
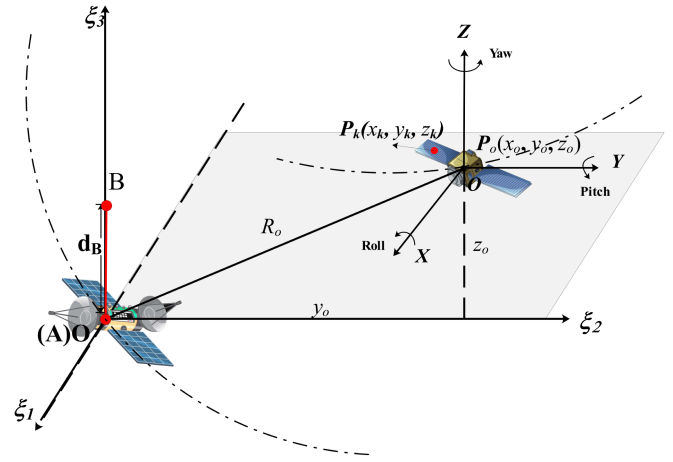

Fig. 1. Space-borne InISAR system geometry with compact antenna configuration.

enhancing the ISAR images' resolution, which suppresses the angle glint. The effectiveness of the proposed method in suppressing the angle glint is verified by the simulation result.

The rest of this article is organized as follows. In Section II, the system geometry configuration and signal model for the InISAR system are introduced. The PFA and SO-LPFT processing and 3-D imaging are introduced in Section III. In addition, in Section IV, performance of the proposed method is examined using simulation data. Finally, Section V concludes this article.

II. IMAGING MODEL

A. System Configuration and Imaging Geometry

Fig. 1 shows the InISAR system geometry with compact antenna configuration, in which the "antenna axis" is denoted along the ξ_3-axis.

The radar observation coordinate system is $O\xi_1\xi_2\xi_3$. The point O represents the center of $O\xi_1\xi_2\xi_3$. To construct a phase interferometer, the antenna pair (antennas A and B) are arranged along the altitude dimension, i.e., ξ_3-axis. Fig. 1 shows that the antenna A is placed in the center of the coordinate system $O\xi_1\xi_2\xi_3$, which is a transmitter and a receiver at the same time. The receive antenna B, is placed with its baseline length to the origin at d_B and placed along the xi_3-axis.

The coordinate system of the target body expressed as $OXYZ$ is parallel to $O\xi_1\xi_2\xi_3$ initially.

At the beginning, P_o denotes the center of the target body coordinate system. In the radar coordinate system, the location of P_o is $\boldsymbol{X_o} = (X_o, Y_o, Z_o)$. According to this, the range between the radar and target can be represented as $R_o = \sqrt{X_o^2 + Y_o^2 + Z_o^2}$ at the starting time. $\boldsymbol{P_k} = (x_k, y_k, z_k)$ represents an arbitrary scatterer k on the target body. $\boldsymbol{P_k(0)} = (x_k(0), y_k(0), z_k(0))$ represents the initial position of the kth scatterer. R_{nk} represents the initial range between each receiver and $P_k(0)$, where n runs through the symbols for the receive antennas ($n = A, B$).

In this geometry, we assume that the first component of $\boldsymbol{\Omega}_{\text{total}}$ in the ξ_1 frame is 0. Thus, we define the rotational vector as

$$\boldsymbol{\Omega}_{\text{total}} = (0, \Omega_2, \Omega). \tag{1}$$

B. Signal Model

The radar antenna A is set up to transmit a wideband linear frequency modulation (LFM) signal, which can be denoted as

$$S(t) = \text{rect}\left(\frac{t}{T_p}\right) \cdot \exp\left[j2\pi\left(f_c t + \frac{k_w}{2}t^2\right)\right] \tag{2}$$

where the transmitted signal's envelope is denoted by $\text{rect}(\cdot)$, the chirp rate of the transmitted signal is represented as k_w, the pulsewidth is represented as T_p, the carrier frequency is represented as f_c, and the fast time is represented as t.

Regarding the target as the model with multiscatterers, and the kth scatterer's reflectivity coefficient is σ_k, we adopt the dechirp technology to receive signal . Then, the compressed LFM signal can be obtained. The range-compressed echo in range-frequency azimuth-time domain by the receiver n is written as

$$
\begin{aligned}
&S_n(f_r, t_a) \\
&= \sigma_k \cdot \text{sinc}\left[T_p\left(f_r + \frac{k_w}{c}(\Delta R_{Ak}(t_a) + \Delta R_{nk}(t_a))\right)\right] \\
&\quad \cdot \exp\left[-j2\pi\frac{f_c + f_r}{c}(\Delta R_{Ak}(t_a) + \Delta R_{nk}(t_a))\right]
\end{aligned} \tag{3}
$$

where f_r denotes the range frequency and c is the light speed. $\Delta R_{nk}(t_a)$ ($n=$ A or B) represents the instantaneous range difference at the slow time t_a from the reference point O to the kth scatterer P_k. $R_{nk}(t_a)$ is expressed as

$$\Delta R_{nk}(t_a) = R_{nk}(t_a) - R_{no}(t_a) \tag{4}$$

where $R_{nk}(t_a)$($n=$ A, B) represents the instantaneous range between the location of kth scatterer and the receive antenna n at the slow time t_a. $R_{nk}(t_a)$ is expressed as

$$R_{nk}(t_a) = |\boldsymbol{X_k}(\boldsymbol{t_a}) - \boldsymbol{X_n}| \tag{5}$$

where $\boldsymbol{X_n}$($n=$ A, B) represent the coordinates of the receiver n in the radar coordinate $O\xi_1\xi_2\xi_3$. In particular, $\boldsymbol{X_o} = (X_o, Y_o, Z_o)$, $\boldsymbol{X_A} = (0, 0, 0)$, and $\boldsymbol{X_B} = (0, 0, d_B)$. Then, (4) can be rewritten as

$$\Delta R_{nk}(t_a) = |\boldsymbol{X_k}(\boldsymbol{t_a}) - \boldsymbol{X_n}| - |\boldsymbol{X_o}(\boldsymbol{t_a}) - \boldsymbol{X_n}| \tag{6}$$

where

$$\boldsymbol{X_k}(\boldsymbol{t_a}) = \boldsymbol{X_o} + \boldsymbol{P_k}(\boldsymbol{t_a}) \tag{7}$$

represents the instantaneous coordinate of the scatterer k at the slow time t_a in the radar coordinate system. $\boldsymbol{P_k}(\boldsymbol{t_a}) = (x_k(t_a), y_k(t_a), z_k(t_a))$ represents the instantaneous coordinate of the scatterer k at slow time t_a in the coordinate system $OXYZ$. The 2-D ISAR image formation depends on the geometric transform relation between the radar and the target, which projects the target onto the image projection plane (IPP). The location of the scatterer k in the IPP can be calculated by

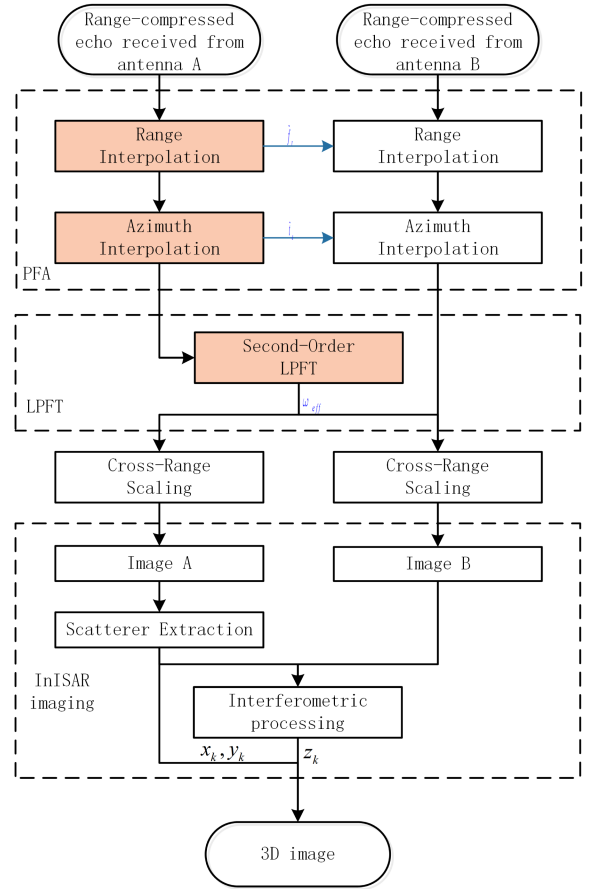$$\boldsymbol{P_k}(\boldsymbol{t_a}) = (\boldsymbol{M_\Omega} \cdot \boldsymbol{P_k}(\boldsymbol{0})^T)^T. \tag{8}$$

Fig. 2. InISAR 3-D imaging flow chart under large rotational angle.

Based on the principle of vector synthesis, $\boldsymbol{\Omega}_{\text{total}}$ defines the synthetic total rotational vector [3]. Since the motion along the RLOS cannot affect the Doppler frequency and IPP, we obtain the effective rotation $\boldsymbol{\Omega}$ by projecting the total rotation vector $\boldsymbol{\Omega}_{\text{total}}$ onto the vertical direction of RLOS. Thus, rotational matrix $\boldsymbol{M_\Omega}$ can be defined as

$$\boldsymbol{M_\Omega} = \begin{bmatrix} \cos(\theta) & \sin(\theta) & 0 \\ -\sin(\theta) & \cos(\theta) & 0 \\ 0 & 0 & 1 \end{bmatrix} \tag{9}$$

where θ denotes the rotational angle formed by the rotational vector perpendicular to line-of-sight (LOS), which is constituted by θ_{ra} and θ_{rot}. θ_{ra} is produced by the radar flight and θ_{rot} is produced by the target rotation. ω_{ra} and ω_{rot} denotes the corresponding angular velocities. Most space targets, such as slowly rotating satellites, are stably rotating around a fixed axis. Thus, θ can be represented as

$$
\begin{aligned}
\theta &= \theta_{ra} + \theta_{\text{rot}} \\
&= \omega_{\text{ra}} \cdot t_a + \omega_{\text{rot}} \cdot t_a.
\end{aligned} \tag{10}
$$

III. 3-D IMAGING ALGORITHM FOR LARGE ROTATIONAL ANGLE

At the start of this section, we discuss the image defocus caused by large rotational angles, i.e., MTRC and DFM. To avoid
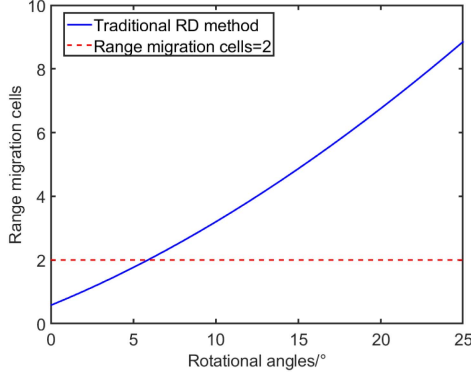
Fig. 3.   MTRC values versus rotational angles.

Fig. 4.   Result of MTRC after (a) range compression, (b) range interpolation, and (c) azimuth interpolation.

its impact, we employ PFA and SO-LPFT to eliminate MTRC and DFM, respectively. Meanwhile, the cross-range scaling is accomplished. In addition, the coordinates of the scatterers in the vertical and horizontal dimensions are extracted from the focused and scaled ISAR image. Finally, the altitude coordinates are calculated from interferometric phase extracted from the two high-resolution images. The 3-D images of space targets are formed. Fig. 2 shows the flow diagram of the 3-D imaging algorithm for a large rotational angle.

In order to demonstrate that for what values of the large rotational angle the effects of MTRC cannot be neglected, we analyzed the MTRC of the scatterer (5,10,5) for different rotational angles, as shown in Fig. 3 .

As shown in Fig. 3, with the increase of the rotational angle, the MTRC increases gradually and becomes comparable to two range cells when the rotational angle is larger than $6°$. When the rotational angle exceeds $15°$, the MTRC is about five range cells, which is not a negligible impact for the ISAR imaging. Thus, we propose the ISAR imaging method under large rotational angle, which can eliminate the MTRC and DFM caused by the large rotational angle.

A. MTRC Elimination Using PFA

Substituting (4)–(9) into (3), the signal received by receiver $n(n=A, B)$ is rewritten as (11) shown at the bottom of this page, where R_{cn} represent the constant term and $\text{sinc}[E_n]$ denotes the synthetic range envelope of the receiver $n(n=A, B)$.

$$
\begin{cases}
R_{cA} = \frac{1}{2}\left(R_{nk}^2 + Z_o \cdot z_k(0)\right) \\
R_{cB} = \frac{1}{2}\left(R_{nk}^2 + Z_o \cdot z_k(0) - 2d_B z_k(0)\right) \\
E_A = T_p\left(f_r + \frac{k_w}{c}(2\Delta R_{Ak}(t_a))\right) \\
E_B = T_p\left(f_r + \frac{k_w}{c}(\Delta R_{Ak}(t_a) + \Delta R_{Bk}(t_a))\right).
\end{cases}
\tag{12}
$$

It is noted that θ varies with slow time t_a. In (11), it can be seen that slow time t_a and range frequency f_r are coupling, which causes the MTRC shown in Fig. 4(a). Using (13), (11) can be
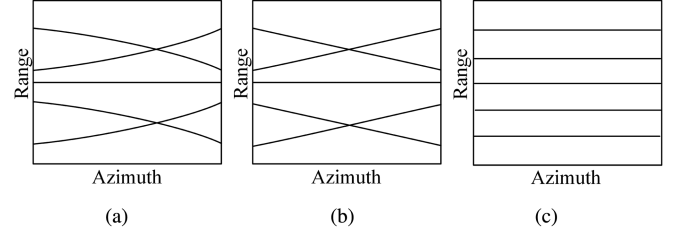
expressed in the spatial frequency domain as follows:

$$
\begin{cases}
F_x = -2\pi \frac{f_c+f_r}{c} \cdot \frac{1}{R_o}\left(X_o \cdot \cos\theta - Y_o \cdot \sin\theta\right) \\
F_y = -2\pi \frac{f_c+f_r}{c} \cdot \frac{1}{R_o}\left(X_o \cdot \sin\theta + Y_o \cdot \cos\theta\right) \\
F_{cA} = -2\pi \frac{f_c+f_r}{c} \cdot \frac{1}{R_o}(R_{cA}) \\
F_{cB} = -2\pi \frac{f_c+f_r}{c} \cdot \frac{1}{R_o}(R_{cB})
\end{cases}
\tag{13}
$$

$$
S_n(F_x, F_y) = \sigma_n \text{sinc}\left[E_n\right]
$$
$$
\cdot \exp\left[j \cdot (F_x \cdot x_k(0) + F_y \cdot y_k(0) + F_{cn})\right]
\tag{14}
$$

The spatial frequency-domain spectrum is not uniform, as shown in the equation of the azimuth spatial frequency F_x and range spatial frequency F_y. To address this issue, the LOS polar to rectangular resampling is used to transform the nonuniform samples into a uniform grid in the spatial frequency domain [18]. In addition, the time-consuming 2-D interpolation issue is often divided into two separate ranges and azimuth resampling using the standard PFA in order to increase the computational efficiency. The aim of the range resampling is to make F_y equally spaced in the range direction. In detail, the range interpolation can be expressed as

$$
f_r = f_c\left(\frac{1}{\cos\theta_{\text{ra}}} - 1\right) + \widetilde{f}_r \frac{1}{\cos\theta_{\text{ra}}}
\tag{15}
$$

where $\widetilde{f}_r$ represents the new range frequency after interpolation. The result of MTRC after the range interpolation is shown in Fig. 4(b). After the range interpolation, (13) can be rewritten as

$$
\begin{cases}
F_x = -2\pi \frac{f_c+\widetilde{f}_r}{c} \cdot \frac{1}{R_o} \cdot (X_o \cdot (\cos\theta_{\text{rot}} - \tan\theta_{\text{ra}}\sin\theta_{\text{rot}}) \\
\quad -Y_o \cdot (\sin\theta_{\text{rot}} + \tan\theta_{\text{ra}}\cos\theta_{\text{rot}})) \\
F_y = -2\pi \frac{f_c+\widetilde{f}_r}{c} \cdot \frac{1}{R_o} \cdot (X_o \cdot (\sin\theta_{\text{rot}} + \tan\theta_{\text{ra}}\cos\theta_{\text{rot}}) \\
\quad +Y_o \cdot (\cos\theta_{\text{rot}} - \tan\theta_{\text{ra}}\sin\theta_{\text{rot}})) \\
F_{cA} = -2\pi \frac{f_c+\widetilde{f}_r}{c} \cdot \frac{1}{R_o \cdot \cos\theta_{\text{ra}}}(R_{cA}) \\
F_{cB} = -2\pi \frac{f_c+\widetilde{f}_r}{c} \cdot \frac{1}{R_o \cdot \cos\theta_{\text{ra}}}(R_{cB}).
\end{cases}
\tag{16}
$$

In the second step of the PFA, the purpose of azimuth resampling is to make F_x evenly spaced along the azimuth direction.

$$
S_n(f_r, t_a) = \sigma_n \text{sinc}[E_n] \cdot \exp\left[-j \cdot \frac{2\pi}{R_o} \cdot \frac{f_c+f_r}{c}\left((X_o \cdot x_k(0) + Y_o \cdot y_k(0)) \cdot \cos\theta + (-Y_o \cdot x_k(0) + X_o \cdot y_k(0)) \cdot \sin\theta + R_{cn}\right)\right]
\tag{11}
$$

The operation of the azimuth resampling is clarified as

$$t_a = \frac{f_c}{f_c + \widetilde{f}_r} \cdot \widetilde{t}_a \qquad (17)$$

where $\widetilde{t}_a$ represents the new azimuth time variable.

After resampling, the signal turns to (18) shown at the bottom of this page. After the Taylor approximation, the signal can be rewritten as (19) shown at the bottom of this page. Comparing (11) with (19), the term $\frac{f_c + f_r}{c}$ in (11) becomes $\frac{1}{\lambda}$ in (19), and the MTRC is rectified, which is shown in Fig. 4(c).

B. Chirp Rate Estimation and Compensation by SO-LPFT

According to the aforementioned analysis, the MTRC is eliminated by decoupling the range frequency f_r and azimuth time t_a, which is demonstrated in (19). In (19), the quadratic term remains, causing the azimuth defocusing. In order to acquire the well-focused ISAR imagery, the SO-LPFT is employed to (19), which can be written as (20) shown at the bottom of this page.

Once the estimated rotational angular velocity $\widehat{\omega}_{\rm rot}$ satisfies the requirement of the estimation accuracy, (20) can be represented as (21) shown at the bottom of this page. Comparing (19) with (21), the quadratic term in (19) is compensated. At this point, the integral in (21) can be regarded as a typical Fourier transform. And a well-focused image is obtained.

Thus, the key to focus the image is estimating the rotational angular velocity accurately. In reality, the focusing degree of the image is selected as an indicator to describe the estimation accuracy of $\widehat{\omega}_{\rm rot}$. The commonly used image characteristic is contrast, represented as

$$\widehat{\omega}_{\rm rot} = \underset{\omega_{\rm rot}}{\arg\max} \left\| C \left({\rm Image}_A \left(\widetilde{f}_r, \widetilde{t}_a, \omega_{\rm rot} \right) \right) \right\| \qquad (22)$$

where the image contrast can be calculated by

$$C({\rm Image}_A) = \frac{\sqrt{\left(|{\rm Image}_A| - \overline{|{\rm Image}_A|} \right)^2}}{\overline{|{\rm Image}_A|}} \qquad (23)$$

where the mean operation is denoted by $(\overline{\cdot})$. Note that the image contrast is defined as the image (amplitude) standard deviation over the image mean value.

After PFA and SO-LPFT processing, the individual scatterers are more clearly in focus. The high-quality well-focused ISAR image can be obtained. Thus, 2-D peak detection is more accurate for improving the precision of interferometric processing.

It is important to notice that the joint PFA and SO-LPFT are adopted to make them less computationally complex . Meanwhile, the interferometric phases are preserved. The resampled range frequency $\widetilde{f}_r$ and azimuth time $\widetilde{t}_a$ in the echo received by antenna A are calculated first. Then, they are used for 2-D interpolation for the echo received by antenna B directly. Similar to this, SO-LPFT is employed to estimate the rotating angular velocity $\widehat{\omega}_{\rm rot}$ in the signal received by the antenna A, which is then utilized to compensate the error in the signal received by the antenna B.

C. 3-D Image Reconstruction

After processing echo received by the antennas A and B, the focused ISAR image A and image B can be obtained as follows:

$$
{\rm Image}_A = \sigma_A {\rm sinc}\,[E_A] \exp\left\{ j\frac{2\pi}{\lambda} \left(R_{CA} \right.\right.
$$

$$
\left.\left. + X_o x_k(0) + Y_o y_k(0) + y_k(0) \right) \right\}
$$

$$
{\rm Image}_B = \sigma_B {\rm sinc}\,[E_B] \exp\left\{ j\frac{2\pi}{\lambda} \left(R_{CB} \right.\right.
$$

$$
S_A(\widetilde{f}_r, \widetilde{t}_a) = \sigma_A {\rm sinc}\,[E_A] \cdot \exp\left[j \cdot \frac{2\pi}{\lambda R_o} \left(\left(X_o(\cos\theta_{\rm rot} - \omega_{\rm ra}\widetilde{t}_a \sin\theta_{\rm rot}) - Y_o(\sin\theta_{\rm rot} + \omega_{\rm ra}\widetilde{t}_a \cos\theta_{\rm rot}) \right) \cdot x_k(0) \right.\right.
$$

$$
\left.\left. + \left(X_o(\sin\theta_{\rm rot} - \omega_{\rm ra}\widetilde{t}_a \cos\theta_{\rm rot}) + Y_o(\cos\theta_{\rm rot} + \omega_{\rm ra}\widetilde{t}_a \sin\theta_{\rm rot}) \right) \cdot y_k(0) + \frac{1}{2}\left(R_{nk}^2 + Z_o z_k(0) \right) \sqrt{1 + \omega_{\rm ra}^2 \widetilde{t}_a^2} \right) \right] \qquad (18)
$$

$$
S_A(\widetilde{f}_r, \widetilde{t}_a) = \sigma_A {\rm sinc}\,[E_A] \cdot \exp\left[j \cdot \frac{2\pi}{\lambda R_o} \left((X_0 x_k(0) + Y_0 y_k(0) + \frac{1}{2}(R_{nk}^2 + Z_o z_k(0))\sqrt{1 + \omega_{\rm ra}^2 \widetilde{t}_a^2}) \right.\right.
$$

$$
\left.\left. + (X_0 y_k(0) - Y_0 x_k(0)) \cdot \omega_{\rm rot}\widetilde{t}_a - \frac{1}{2}(X_0 x_k(0) + Y_0 y_k(0))(\omega_{\rm rot}^2 + \omega_{\rm ra}\omega_{\rm rot}) \cdot \widetilde{t}_a^2 \right) \right]. \qquad (19)
$$

$$
{\rm Image}_A(\widetilde{f}_r, \widetilde{f}_a) = \int S_A(\widetilde{f}_r, \widetilde{t}_a) \cdot \exp\left[j\frac{2\pi}{\lambda R_o} \left(\frac{1}{2}(X_0 x_k(0) + Y_0 y_k(0))(\omega_{\rm rot}^2 + \omega_{ra}\omega_{\rm rot}) \cdot \widetilde{t}_a^2 \right) \right] d\widetilde{t}_a \qquad (20)
$$

$$
{\rm Image}_A(\widetilde{f}_r, \widetilde{f}_a) = \sigma_A {\rm sinc}\,[E_A] \cdot \int \exp\left[j \cdot \frac{2\pi}{\lambda R_o} \left((X_0 x_k(0) + Y_0 y_k(0)) \right.\right.
$$

$$
\left.\left. + \frac{1}{2}(R_{nk}^2 + Z_o z_k(0))\sqrt{1 + \omega_{ra}^2 \widetilde{t}_a^2}) + (X_0 y_k(0) - Y_0 x_k(0)) \cdot \omega_{\rm rot}\widetilde{t}_a \right) \right] d\widetilde{t}_a. \qquad (21)
$$

$$+X_o x_k(0) + Y_o y_k(0) + y_k(0)) \Big\} \qquad (24)$$

where

$$\begin{cases} R_{CA} = \frac{1}{2R_o} \left(R_{nk}^2 + Z_o z_k(0) \right) \\ R_{CB} = \frac{1}{2R_o} \left(R_{nk}^2 + Z_o z_k(0) - 2\mathrm{d}_B z_k(0) \right). \end{cases} \qquad (25)$$

When the peak extraction and cross-range scaling are finished, the target coordinates in horizontal and vertical dimensions in the ISAR image are extracted by

$$\begin{cases} \mathrm{pixel}_x = \frac{\lambda}{2\theta} \\ \mathrm{pixel}_y = \frac{c}{2B_w} \end{cases} \qquad (26)$$

where pixel_x and pixel_y denote the resolution of the range domain and azimuth domain, respectively. Next, we employ interferometric technology [19] to calculate the coordinates in the altitude domain, which can be expressed as

$$\begin{aligned} \Delta\varphi_{AB} &= \mathrm{Angle} \ (\mathrm{Image}_A \cdot \mathrm{Image}_B) \\ &= \frac{2\pi}{\lambda} \left(R_{CA} - R_{CB} \right) \\ &= \frac{2\pi}{\lambda} \frac{d_B}{R_o} z_k(0) \end{aligned} \qquad (27)$$

where * represents the conjugate operation, angle$(\cdot)$ represents the phase radian value, and $\mathrm{Image}_n \ (n = A, B)$ denote the image results obtained by the proposed method.

Thus, the altitude coordinate is calculated by

$$z_k(0) = \frac{\lambda R_o}{2\pi d_B} \cdot \mathrm{angle}(\mathrm{Image}_A \cdot {}^*\mathrm{Image}_B). \qquad (28)$$

Finally, the calculated altitude coordinates are combined with the acquired vertical and horizontal coordinates to form a 3-D InISAR image.

IV. EXPERIMENT ANALYSIS

In this part, several simulation experiments are performed for demonstrating the capability of the proposed method.

A. Simulation Parameters

Initially, the center of the coordinate system $OXYZ$ in the radar observation system is placed at (X_o, Y_o, Z_o), where $X_o = Z_o = 0$ km and $Y_o = 10$ km. The relative velocity of the target and radar is 80 m/s. The simulation parameters of the InISAR system are listed in Table I.

We adopt an evaluation measure to assess the performance in order to quantitatively assess the 3-D image quality. The error of 3-D coordinates of the reconstructed scatterer k is expressed by the Euler distance between the reconstruction coordinate $(\hat{x}_k(0), \hat{y}_k(0), \hat{z}_k(0))$ and the real coordinate $(x_k(0), y_k(0), z_k(0))$. The reconstruction error of the 3-D image is calculated using the average of all scatterers' reconstruction errors, which is written as E_{3D}. The estimation errors are calculated in accordance with the absolute differences in the effective rotational velocity.

TABLE I
RADAR PARAMETERS

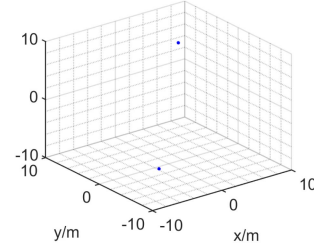| Parameters	Values
Wavelength λ	0.03 m
Carrier frequency f_c	10 GHz
Pulse width T_p	10 μs
PRF	1000 Hz
Range band width B_w	3 GHz
Baseline length d_B	2.5 m
Range difference R_o	10 km
Rotational angle	15°

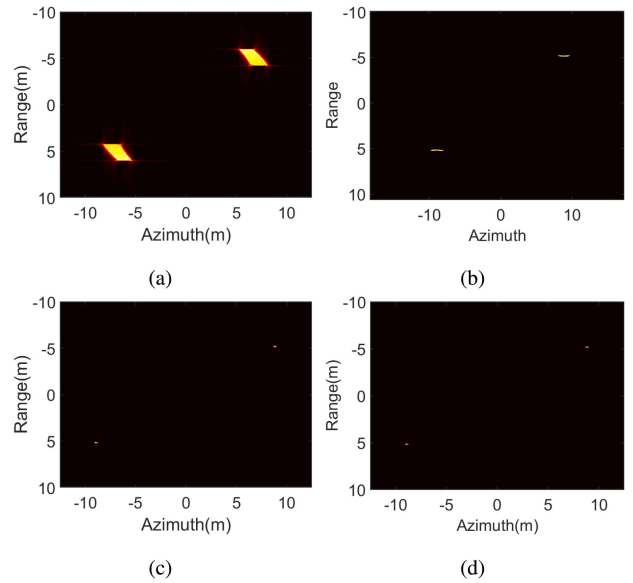Fig. 5. Location of point targets.

Fig. 6. ISAR image obtained by (a) RD method (antenna A), (b) PFA (antenna A), (c) proposed method (antenna A), and (d) proposed method (antenna B).

B. Experiments I

We considered two point targets as shown in Fig. 5, which are located in (-6, -6, -6) and (6, 6, 6), respectively.

Fig. 6 shows the ISAR image by the RD technique, PFA, and the proposed methods. Since MTRC and DFM are ignored, it is shown in Fig. 6(a) that the image obtained by the RD technique is defocused. Consequently, the 3-D reconstruction using the RD approach will show more spurious scatterers, which degrades the image quality. The results in Fig. 6(b) and (c) show that the PFA eliminates MTRC, and SO-LPFT reduces the azimuth defocusing. The high-resolution and well-focused ISAR image is generated using the proposed method, as shown in Fig. 6(c) and (d).
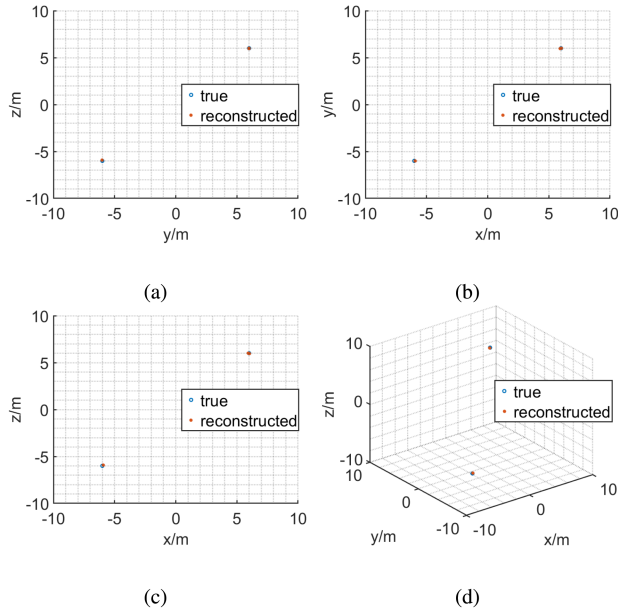
Fig. 7.   Target 3-D images in (a) main view, (b) top view, (c) side view, and (d) 3-D view.

TABLE II
RUNNING TIME

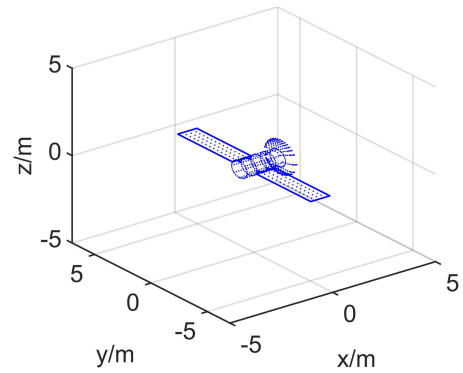| Method	Running time	
	2-D imaging	2-D imaging
RD	0.45 s	7.68 s
PFA	4.217 s	11.97 s
Proposed method	5.234 s	7.46 s

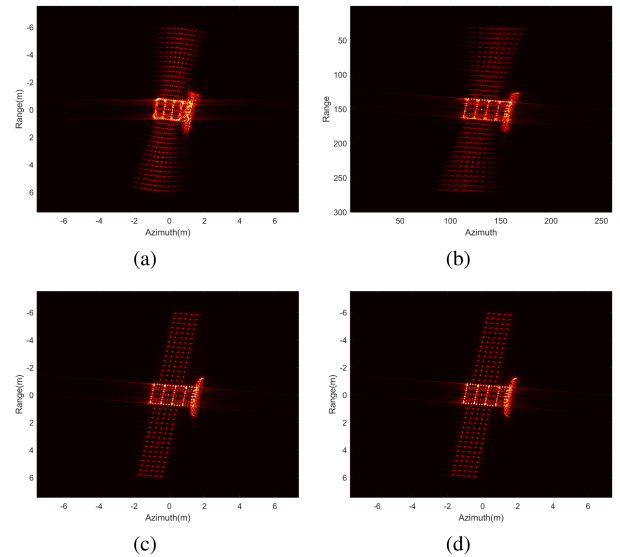Fig. 8.   Scatterer model of Lacrosse.

Fig. 9.   ISAR image of the Lacrosse Satellite model obtained by: (a) RD method (antenna A), (b) RD method (antenna B), (c) proposed method (antenna A), and (d) proposed method (antenna B).

Fig. 7(a) displays the 3-D reconstruction result of the target. Fig. 7(b)–(d) displays the images of the target in three different views. The averaged reconstruction error E_{3D} of the proposed method is 0.00709 m. It can be seen that almost all reconstructed targets coincide with the ideal locations.

The running times for each method in 2-D imaging and 3-D imaging are shown in Table II. It is noted that the result of the running time is obtained by a computer of "Intel Core i5 CPU, 2.9 GHz, memory 16 GB." The running time can be further optimized by the parallel processing in the hardware platform. In Table II, the proposed method still satisfies the real-time performance. It can be seen that the proposed method runs a little longer in 2-D imaging. However, we would like to stress that the results obtained by the RD and PFA are based on three times scatterer extractions in InISAR imaging, which is much more time consuming. In the proposed method, the parameters needed by the 3-D imaging can be acquired by antenna A and shared to antenna B, leading to less computation, as shown in the last row of Table II.

In conclusion, using the proposed method not only leads to the acquisition of high-resolution 2-D images but also obtains 3-D images with more complete information. Thus, more accurate 3-D reconstruction results can be obtained without extra time consumption.

C. Experiments II

To better explain the necessity of high resolution, in this part, we simulate our proposed method using the scatterer model of the Lacrosse satellite, a more complicated satellite target. The model is 12 m long and 3.2 m wide modeled by 679 scatterers as shown in Fig. 8. There are over hundreds of scatterers in this model, while the distance between each scatterer is about 0.05 m, which requires high-resolution image to make the scatterers separated well.

The 2-D ISAR imaging results of the Lacrosse satellite target model are shown in Fig. 9, where Fig. 9(a) and (b) is obtained by the RD method, and Fig. 9(c) and (d) is obtained by the proposed method. It is seen from Fig. 9(a) and (b) that images are defocused as a result of the high relative rotational angle of the space target, while all scatterers of the target are well focused in Fig. 9(c) and (d) by the proposed method.

Fig. 10(a)–(c) displays the 3-D reconstruction results of the Lacross model produced by the conventional method, PFA, and the presented method, respectively. The displays of different views in 3-D results of Fig. 10(a) are shown in Fig. 11(a)–(d),
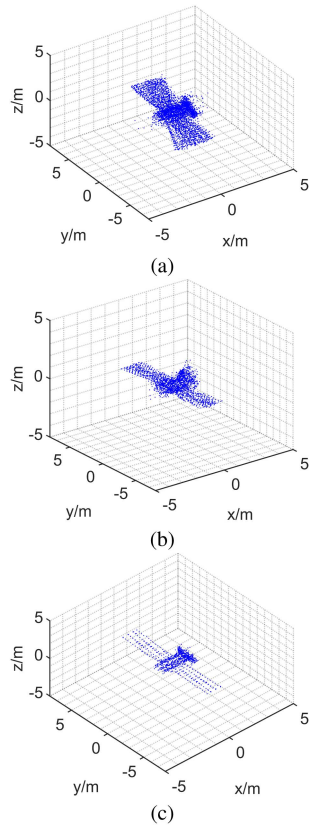
Fig. 10. 3-D reconstruction results of the Lacross model obtained by (a) traditional RD method, (b) PFA, and (c) proposed method.
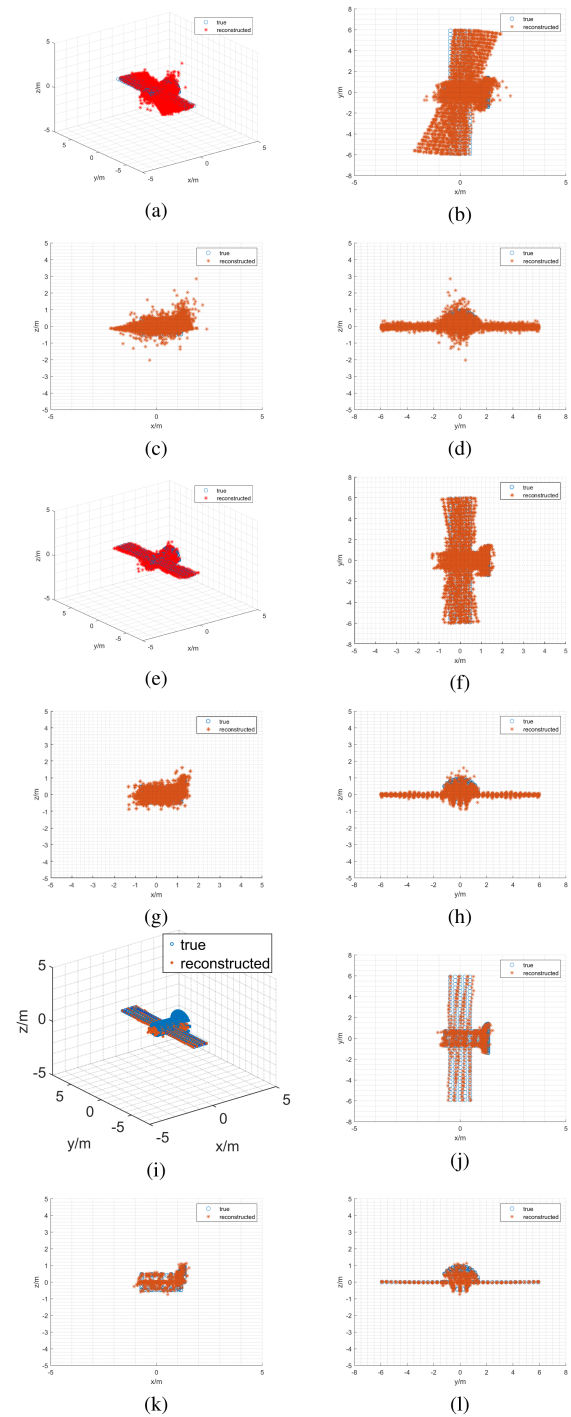

Fig. 11. 3-D reconstruction results of the Lacross model in different views obtained by (a)–(d) traditional RD, (e)–(h) PFA, and (i)–(l) proposed method.

the different views in Fig. 10(b) are shown in Fig. 11(e)–(h), and the different views in Fig. 10(c) are shown in Fig. 11(i)–(l). Fig. 11(a), (e), and (i) displays the comparison of 3-D reconstruction results and the true condition of the target obtained by the typical RD, PFA, and proposed method. Fig. 11(b)–(d), (f)–(h), and (j)–(l) shows the images of the target in different views obtained by the typical RD, PFA, and the proposed method, respectively, which verifies that the proposed method offers high precision in accordance with the estimated scatterer positions. The average reconstruction error E_{3D} of the traditional RD method is 0.357 m, the average reconstruction error E_{3D} of the PFA is 0.0466 m, and the average reconstruction error E_{3D} of the proposed method is 0.0085 m. The comparisons verify that the proposed method offers high precision in accordance with the estimated scatterer positions.

From Fig. 10(a), it can be seen that the outline of 3-D reconstruction images generated by the traditional method is blurring and unrecognizable since more false scatterers appear. In contrast with the result of Fig. 10(a), the image in Fig. 10(b) is sharp in all of the three dimensions. The proposed method has a convincing performance, as evidenced by the fact that the defocused problem in Fig. 10(a) is successfully addressed and the shape of the Lacross model is now much clearer.

D. Experiment III

In this part of the experiment, we deal with the robust performance of the proposed method. In detail, the values of the relative rotational angle for which the proposed method is more effective than the traditional 3-D InISAR method are carefully discussed.

Figs. 12–14 show the 2-D image and 3-D reconstruction result comparison of the typical RD method, PFA method, and the presented method. Fig. 12(a), (f), and (k) shows the ISAR images under the relative rotational angle of 2°. Fig. 12(a) is the ISAR image of the RD method, Fig. 12(f) is the ISAR image of the
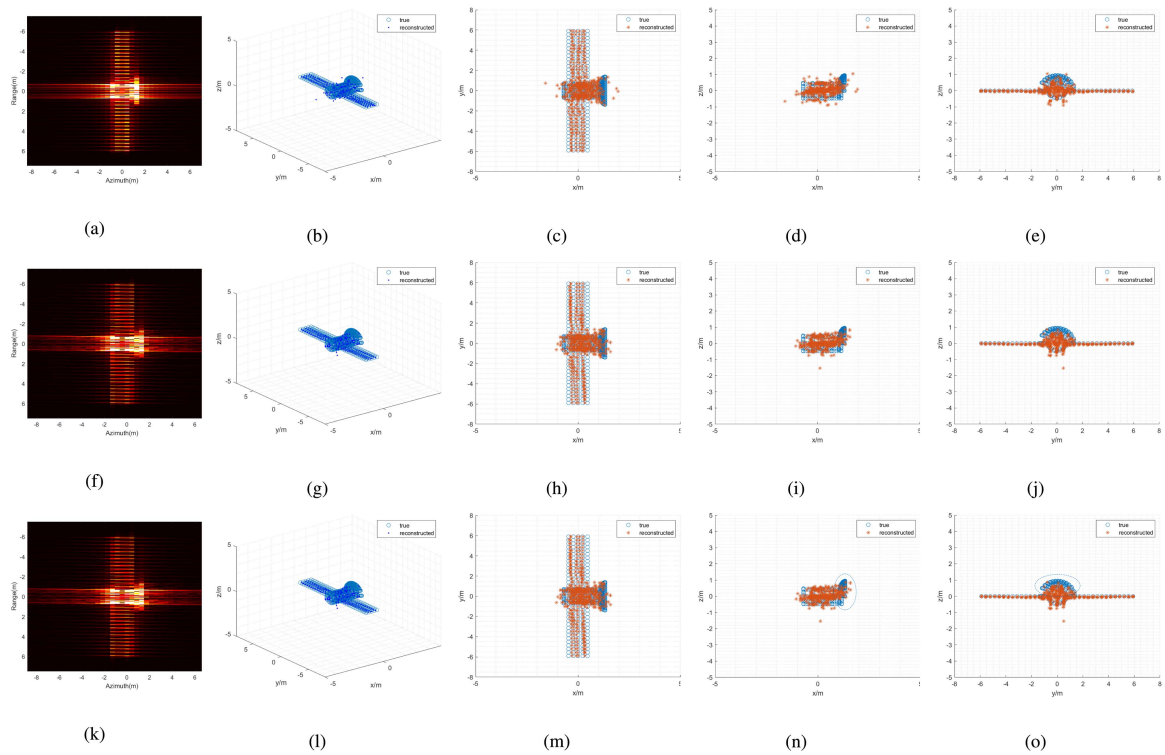
Fig. 12.　ISAR image and 3-D reconstruction results of the Lacross model obtained by (a)–(e) traditional RD, (f)–(j) PFA, and (k)–(o) proposed method under rotational angle of 2°.
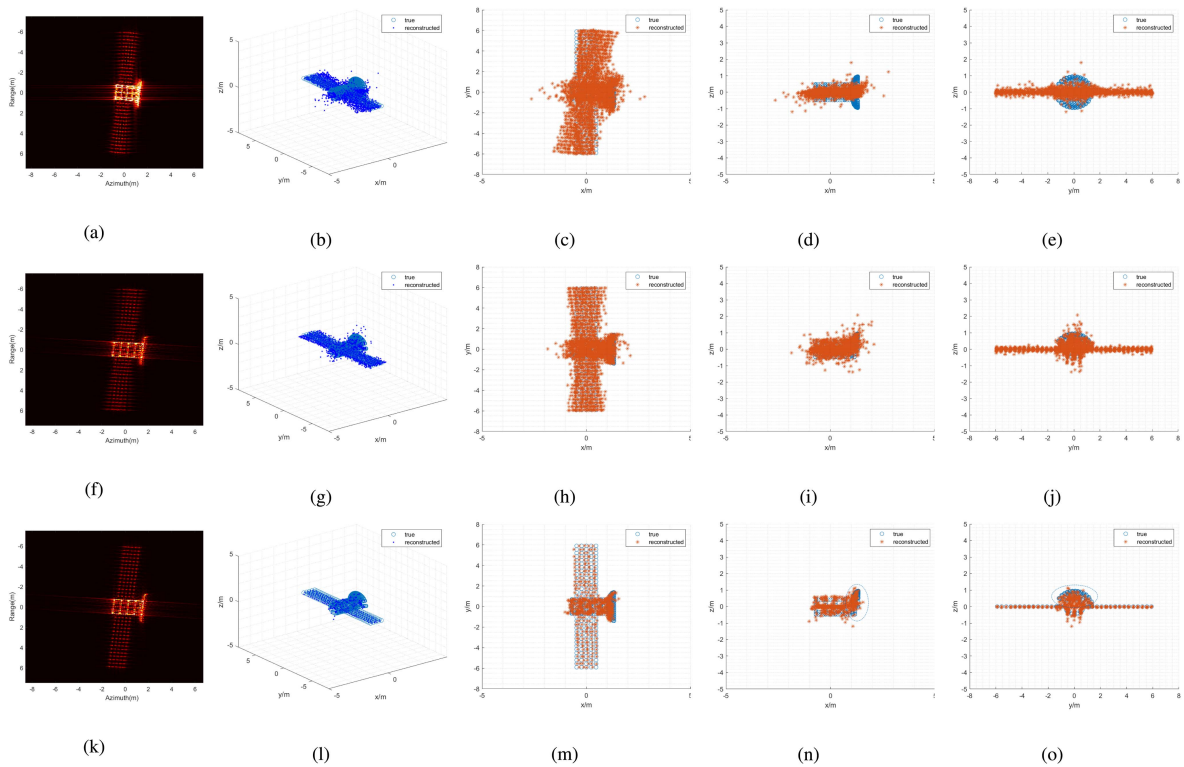

Fig. 13.　ISAR image and 3-D reconstruction results of the Lacross model obtained by (a)–(e) traditional RD, (f)–(j) PFA, and (k)–(o) proposed method under rotational angle of 10°.
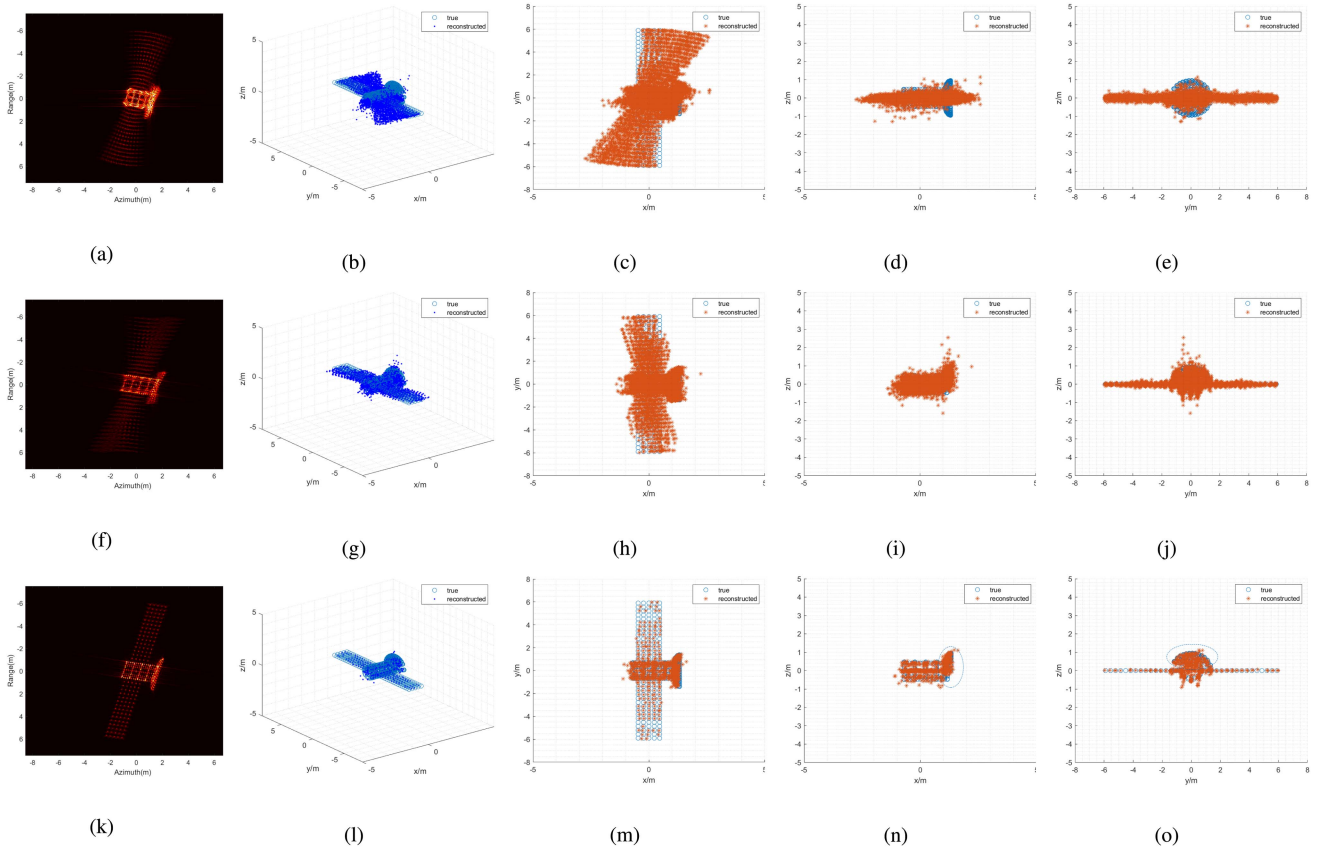
Fig. 14. ISAR image and 3-D reconstruction results of the Lacross model obtained by (a)–(e) traditional RD, (f)–(j) PFA, and (k)–(o) proposed method under rotational angle of 25°.

PFA, and Fig. 12(k) is the ISAR image of the proposed method. Fig. 12(b)–(e) shows 3-D reconstruction results of the traditional RD method, Fig. 12(g)–(j) shows 3-D reconstruction results of the PFA, and Fig. 12(k)–(o) shows 3-D reconstruction results of the proposed method. From the comparison of Fig. 12(a), (f), and (k), the advantage of the proposed method is not obvious under the relative rotational angle of 2°. It is noted that several scatterers cannot be reconstructed due to the limited resolution.

Fig. 13(a), (f), and (k) shows the ISAR images under the relative rotational angle of 10°. Fig. 13(a) is the ISAR image of the RD method, Fig. 13(f) is the ISAR image of the PFA, and Fig. 13(k) is the ISAR image of the proposed method. From the comparison of Fig. 13(a) and (k), it is clear that the relative rotational angle influences the ISAR image in Fig. 13(a), resulting in the MTRC and Doppler defocus. Fig. 13(b)–(e) shows 3-D reconstruction results of the traditional RD method, Fig. 13(g)–(j) shows 3-D reconstruction results of the PFA, and Fig. 13(k)–(o) shows the 3-D reconstruction results of the proposed method. Due to the defocused ISAR image, the extracted phase information is inaccurate, which leads to the distorted outline in the reconstruction result. From the comparison of Fig. 13(b), (g), and (l), the 3-D result obtained by the proposed method can reconstruct the target accurately. It is apparent that the proposed method has the advantage in high quality 3-D imaging under the relative rotational angle of 10°. It is noted that most of scatterers are reconstructed due to the increased resolution in Fig. 13(h).

Fig. 14(a), (f), and (k) shows the ISAR images under the relative rotational angle of 25°. Similarly, Fig. 14(a) is the ISAR image of the RD method, Fig. 14(f) is the ISAR image of the PFA, and Fig. 14(k) is the ISAR image of the proposed method, respectively. With the increasing relative rotational angle, the defocus of the ISAR image become serious, which is shown in Fig. 14(a). Fig. 14(b)–(e) shows 3-D reconstruction results of the traditional method, Fig. 14(g)–(j) shows the 3-D reconstruction results of the PFA, and Fig. 14(k)–(o) shows 3-D reconstruction results of the proposed method. From the comparison of Fig. 14(d) and (h), the advantage of the proposed method is obvious under the relative rotational angle of 25°. It is noted that all scatters are well reconstructed because the resolution of the ISAR image is improved significantly.

In order to verify the robustness of the proposed method under different relative rotational angles, we performed simulations under different angles. Fig. 15 shows the root mean square errors (RMSEs) of the x, y, and z coordinates of scatterers for different relative rotational angles. Fig. 15(a) shows the RMSEs results obtained by the traditional RD method, Fig. 15(b) shows the RMSEs results obtained by the PFA, and Fig. 15(c) shows the RMSEs results obtained by the proposed method. From the result obtained by the traditional method, it can be seen that the scatterers are well estimated for the angles smaller than 5°, with the RMSE smaller than 0.02 m. When the rotational angle is higher than 5°, the 3-D reconstructed error for the traditional method cannot be neglected. Due to the defocused ISAR image
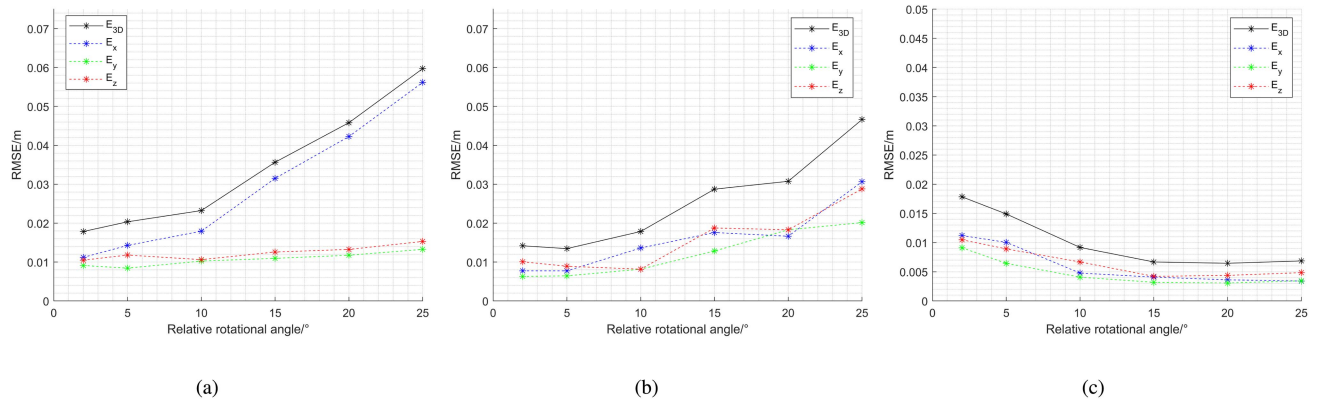
Fig. 15. RMSEs under different rotational angles obtained by (a) traditional RD, (b) PFA, and (c) proposed method.
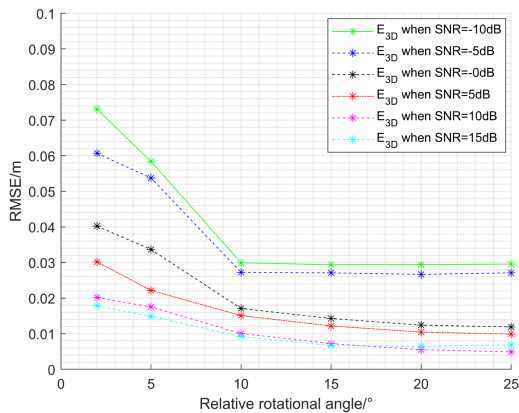

Fig. 16. RMSEs under different SNR.

caused by the increased relative rotational angle, the accuracy of the reconstructed results obtained by the traditional RD method and PFA are influenced when the rotational angle is greater than 5°. However, from the result obtained by the proposed method, the RMSEs of the reconstructed location are no greater than 0.01 m when the rotating angle is larger than 15°, which is efficient even for small target reconstruction. This indicates that the proposed approach can produce reliable results.

As we all known, angle glint is regarded as a limitation of the InISAR imagery. In detail, the altitude coordinates could not be carried out if the projection of two scatters is the same. The assumption of the 3-D InISAR imagery is that a single scatterer exists in each pixel on the 2-D ISAR image. In this article, our work focuses on solving the InISAR imaging problem under a large rotational angle. The proposed method makes the projection of each two scatterers different through enhancing the resolution of the ISAR image, which solves the aforementioned issue. Comparing blue circles in Fig. 12(m)–(0) with blue circles in Figs. 13(m)–(o) and 14(m)–(o), we see the scatters are reconstructed more accurately with the improvement of the resolution. The result in Fig. 15(c) shows that RMSEs are decreasing with the increasement of image resolution, which proves the effectiveness of the proposed method in suppressing the angle glint.
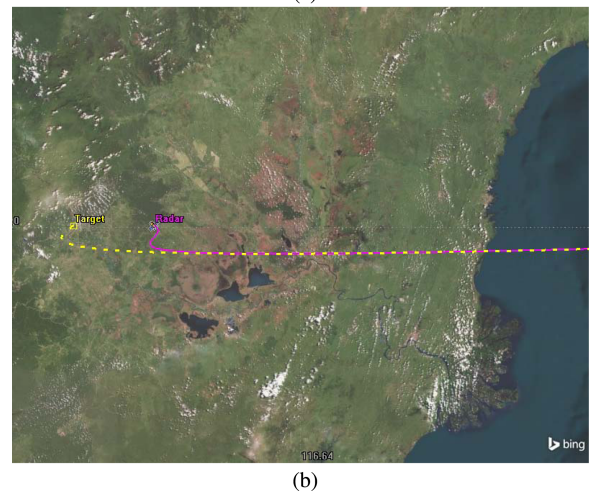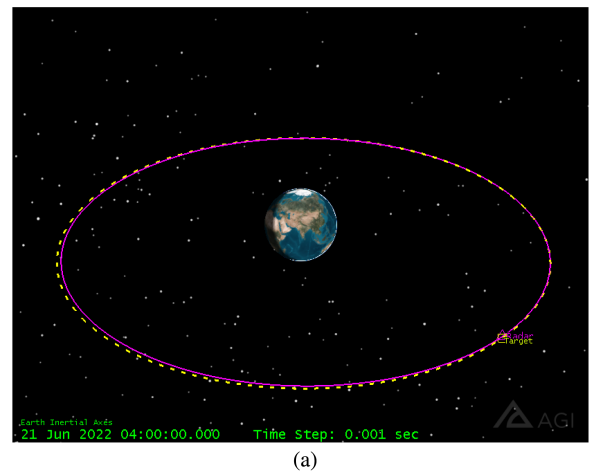

Fig. 17. Trajectories simulation of target and radar (a) 3-D image and (b) 2-D image.

In addition, we give simulation results under different SNRs to verify the antinoise ability of the proposed method. The (RMSEs of 3-D coordinates of scatterers E_{3D} under different SNRs are presented in Fig. 16. Overall, the scatterers are well estimated for the SNR greater than 0 dB, together with the RMSE smaller than 0.04 m. Due to the low quality of the image caused by the high noise level, the extracted interferometric phase is influenced

TABLE III
TRAJECTORIES PARAMETERS OF TARGET AND RADAR

	Radar center	Target center
X(km)	3030.72	3710.7
Y(km)	41655.2	41827.2
Z(km)	0	0
X Velocity(km/s)	-3.04466	-3.04209
Y Velocity(km/s)	0.282143	0.275137
Z Velocity(km/s)	0	0

(a)

(b)
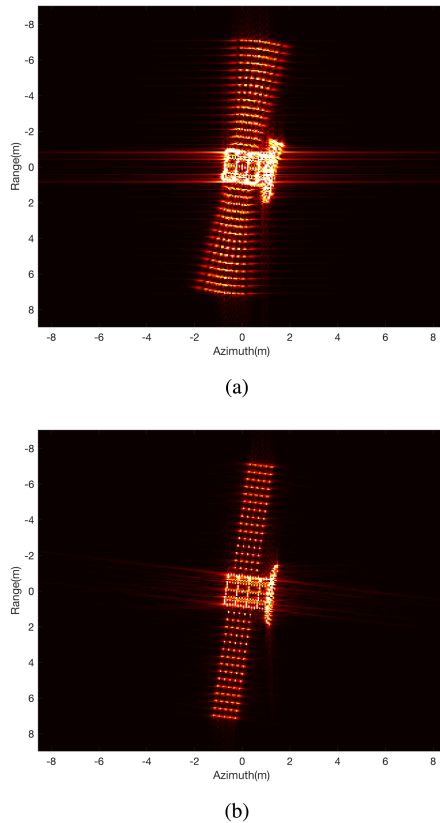
Fig. 18.   2-D image obtained by (a) RD method and (b) proposed method.

(a)   (b)

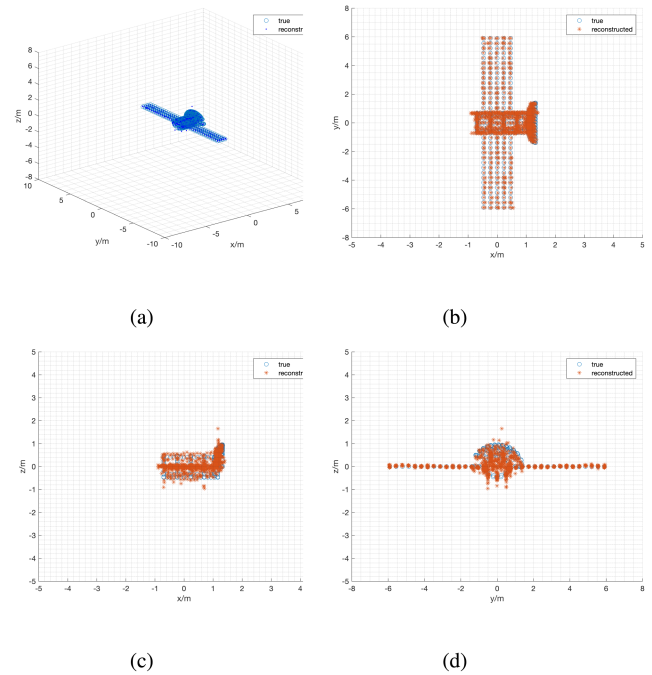(c)   (d)

Fig. 19.   3-D reconstruction image obtained by proposed method (a) 3-D image, (b) top view (c) main view (d) side view under scenario in Fig. 17.
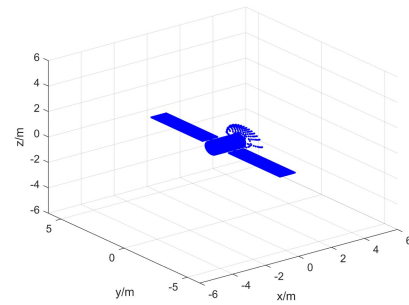

Fig. 20.   Surface Model of Lacrosse.

when the SNR is smaller than 0 dB. Even so, the RMSEs of the reconstructed position are no more than 0.08 m when the SNR is smaller than 0 dB. The results show that the proposed method can offer stable performance in terms of the RMSE of the estimated scatterer positions.

E. Experiment IV

In this section, to verify the performance of the proposed method on the application of this method to image satellites, considering possible actual mutual motion scenarios between a satellite on which the radar system is mounted and the observed satellite. The scenario is simulated by STK, which is widely used in aerospace industry. The simulation scenario of the target and radar is shown in Fig. 17, and orbit parameters of two satellites are shown in Table III .

In this simulation scenario, STK data with a range of 10 km between the radar and the target is selected for echo generation simulation. Then, the proposed method is employed to obtain the focused ISAR image and 3-D image. Besides, the rotational angle of target is set as 15 ° in the 2 s of synthetic aperture time, and the relative rotational angle between target and radar is 0.1318°. Fig. 18(a) and (b) shows the ISAR images obtained by the RD method and proposed method, respectively. Fig. 19(a)–(d) shows the 3-D reconstruction result comparison of the proposed method in the simulation scenario. It can be seen from Fig. 19 that almost all the scatterers are reconstructed in the ideal position. The averaged reconstruction error E_{3D} of the proposed method is 0.0079 m, which demonstrates that the advantage of the proposed method is still obvious under the actual mutual motion scenarios between the target and radar.

F. Experiment V

Considering that the point targets do not seem to be sufficient verification, in this section, we build the surface target for an experiment to better verify the performance of the proposed method. The model of the surface Lacrosse target is shown in Fig. 18. The size of the target in Fig. 20 is the same as the
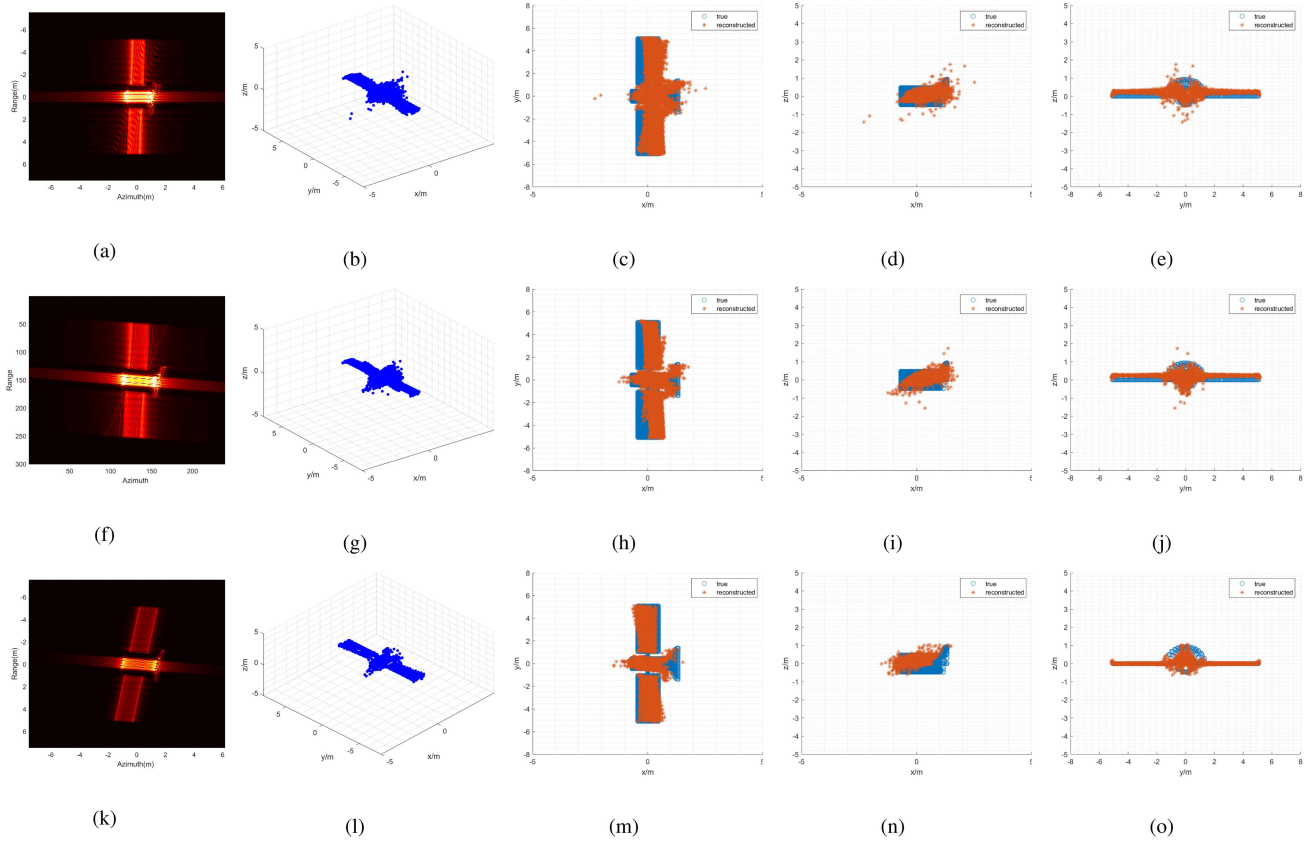
Fig. 21. ISAR image and 3-D reconstruction results of the surface Lacross model obtained by (a)–(e) traditional RD, (f)–(j) PFA, and (k)–(o) proposed method under rotational angle of 25°.

target in Fig. 8. The relative rotational angle in this experiment imaging time is 15°. The ISAR image and 3-D reconstruction results of the surface Lacross model obtained by the traditional RD method, PFA method, and the proposed method are shown in Fig. 19. 3-D reconstruction error E_{3D} of RD is 0.0012 m, E_{3D} of the PFA is 0.0038 m, and E_{3D} of the proposed method is 0.0042 m.

It is seen that Fig. 21(a) is defocused in both range and azimuth dimension, and Fig. 21(f) is defocused in azimuth dimension. The proposed method can obtain the high-resolution ISAR imaging for the simulated surface target. According to the comparison of Fig. 21(b), (g), and (l), the shape of the reconstructed target in Fig. 21(l) is more clear than the reconstructed target in Fig. 21(b) and (g). The comparison of the 3-D reconstruction error E_{3D} verifies the result. In brief, our proposed method can obtain well-focused 2-D ISAR images and 3-D InISAR images.

V. CONCLUSION

To address the issue that 3-D imaging results deteriorate seriously due to the increased rotational angle, we propose a novel InISAR method in this article. First, the PFA and SO-LPFT are integrated to the general RD processing to obtain 2-D high-resolution images under a large rotational angle. Second, the peak extraction and cross-range scaling are combined to obtain the coordinates of targets in vertical and horizontal dimensions, and interference technology is utilized to calculate the altitude coordinate. Finally, the extracted vertical and horizontal coordinates, and the calculated altitude coordinates are adopted to reconstruct the 3-D image. In addition, the high-resolution 3-D image can be acquired by the proposed method while the computational time and the radar system complexity are reduced. The simulation experiments verified the effectiveness of the proposed algorithm.

REFERENCES

[1] H. Yunpeng, L. Kebo, L. Yan'gang, and C. Lei, "Review on strategies of space-based optical space situational awareness," *J. Syst. Eng. Electron.*, vol. 32, no. 5, pp. 1152–1166, 2021.

[2] D. A. Ausherman, A. Kozma, J. Walker, H. Jones, and E. Poggio, "Developments in radar imaging," *IEEE Trans. Aerosp. Electron. Syst.*, vol. AES-20, no. 4, pp. 363–400, Aug. 1984.

[3] L. Wang, O. Loffeld, K. Ma, and Y. Qian, "Sparse ISAR imaging using a greedy Kalman filtering approach," *Signal Process.*, vol. 138, pp. 1–10, 2017.

[4] N. Li, Q. Shen, L. Wang, Q. Wang, Z. Guo, and J. Zhao, "Optimal time selection for ISAR imaging of ship targets based on time-frequency analysis of multiple scatterers," *IEEE Geosci. Remote Sens. Lett.*, vol. 19, 2022, Art. no. 4017505.

[5] X. Hu, N. Tong, J. Wang, S. Ding, and X. Zhao, "Matrix completion-based MIMO radar imaging with sparse planar array," *Signal Process.*, vol. 131, pp. 49–57, 2017.

[6] Y. Wang and Y. Jiang, "Inverse synthetic aperture radar imaging of maneuvering target based on the product generalized cubic phase function," *IEEE Geosci. Remote Sens. Lett.*, vol. 8, no. 5, pp. 958–962, Sep. 2011.

[7] X. Li, X. Bai, and F. Zhou, "High-resolution ISAR imaging and aut-ofocusing via 2D-ADMM-Net," *Remote Sens.*, vol. 13, no. 12, 2021, Art. no. 2326.

[8] S. Wei, J. Liang, M. Wang, J. Shi, X. Zhang, and J. Ran, "AF-AMPNet: A deep learning approach for sparse aperture ISAR imaging and autofocusing," *IEEE Trans. Geosci. Remote Sens.*, 2021, pp. 1–14, Art. no. 5206514.

[9] Y. Wang, J. Rong, and T. Han, "Novel approach for high resolution ISAR/InISAR sensors imaging of maneuvering target based on peak extraction technique," *IEEE Sensors J.*, vol. 19, no. 14, pp. 5541–5558, Jul. 2019.

[10] S. Shao, H. Liu, L. Zhang, P. Wang, and J. Wei, "Noise-robust interferometric ISAR imaging of 3-D maneuvering motion targets with fine image registration," *Signal Process.*, vol. 198, 2022, Art. no. 108578.

[11] T. Biao, L. Zhejun, L. Yongxiang, and L. Xiang, "Review on interferometric ISAR 3D imaging: Concept, technology and experiment," *Signal Process.*, vol. 153, pp. 164–187, 2018.

[12] M. Martorella, D. Staglianò, F. Salvetti, and N. Battisti, "3D interferometric ISAR imaging of noncooperative targets," *IEEE Trans. Aerosp. Electron. Syst.*, vol. 50, no. 4, pp. 3102–3114, Oct. 2014.

[13] G. Xu, M. Xing, X. G. Xia, L. Zhang, Q. Chen, and Z. Bao, "3D geometry and motion estimations of maneuvering targets for interferometric ISAR with sparse aperture," *IEEE Trans. Image Process.*, vol. 25, no. 5, pp. 2005–2020, May 2016.

[14] S. Anger, M. Jirousek, S. Dill, and M. Peichl, "ISAR imaging of space objects using large observation angles," in *Proc. 21st Int. Radar Symp.*, 2021, pp. 1–7.

[15] Y. Wang, R. Cao, and X. Huang, "ISAR imaging of target in the terahertz band via the back-projection algorithm combined with the motion compensation," in *Proc. 6th Asia-Pacific Conf. Synthetic Aperture Radar*, 2019, pp. 1–4.

[16] J. Fu, M. Xing, M. Amin, and G. Sun, "ISAR translational motion compensation with simultaneous range alignment and phase adjustment in low SNR environments," in *Proc. IEEE Radar Conf.*, 2021, pp. 1–6.

[17] R. Gong, L. Wang, and D. Zhu, "A novel approach for squint InISAR imaging with dual-antenna configuration," *Digit. Signal Process.*, vol. 127, 2022, Art. no. 103592.

[18] F. Zuo, J. Li, R. Hu, and Y. Pi, "Unified coordinate system algorithm for terahertz video-SAR image formation," *IEEE Trans. THz Sci. Technol.*, vol. 8, no. 6, pp. 725–735, Nov. 2018.

[19] C. L. Liu, F. He, X. Z. Gao, and L. R. Shen, "Squint-mode InISAR imaging based on nonlinear least square and coordinates transform," *Sci. China Technol. Sci.*, vol. 54, pp. 3332–3340, 2011.

Ling Wang received the B.S. degree in electrical engineering, and the M.S. and Ph.D. degrees in information acquirement and processing from the Nanjing University of Aeronautics and Astronautics, Nanjing, China, in 2000, 2003, and 2006, respectively.

In 2003, she joined the Nanjing University of Aeronautics and Astronautics, where she is currently a Professor with the Department of Information and Communication Engineering. She was a Postdoctoral Research Associate with the Department of Mathematical Sciences and Department of Electrical, Computer, and Systems Engineering, Rensselaer Polytechnic Institute, Troy, NY, USA, from 2008 to 2009. She has authored and coauthored more than 100 publications. Her current research interests include radar, microwave imaging image processing, and intelligent information processing.

Dr. Wang was the recipient of the fellowship of Humboldt Experienced Researchers by Alexander von Humboldt Foundation in 2014 and worked with Prof. O. Loffeld with the University of Siegen, Siegen, Germany, from 2015 to 2016. She was selected into the "Six talent peaks project" of Jiangsu Province in 2014 and the "333 talent project" of Jiangsu Province in 2016, respectively.
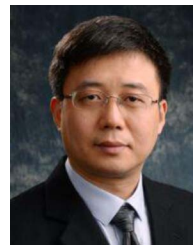
Daiyin Zhu was born in Wuxi, China, in 1974. He received the B.S. degree in electronic engineering from Southeast University, Nanjing, China, in 1996, and the M.S. and Ph.D. degrees in electronic engineering from the Nanjing University of Aeronautics and Astronautics (NUAA), Nanjing, in 1998 and 2002, respectively.

From 1998 to 1999, he was a Guest Scientist with the Institute of Radio Frequency Technology, German Aerospace Center, Weßling, Germany, where he worked in the field of synthetic aperture radar (SAR) interferometry. In 1998, he joined the Department of Electronic Engineering, NUAA, where he is currently a Professor. He has developed algorithms for several operational airborne SAR systems. His research interests include radar imaging algorithms, SAR/inverse synthetic-aperture radar (ISAR) autofocus techniques, SAR ground moving target indication (SAR/GMTI), and SAR interferometry.

Rui Gong was born in Anhui, China, in 1997. She received the B.S. degree in electronics and information engineering from the Kunming University of Science and Technology, Kunming, China, in 2019. She is currently working toward the Ph.D. degree with the Nanjing University of Aeronautics and Astronautics, Nanjing, China, in 2019.

Her research interests include interferometric inverse synthetic aperture radar (InISAR) imaging algorithms and ISAR imaging algorithms.